



# Breaking processes in three-dimensional bonded granular materials with general shapes

S.A. Galindo-Torres\*, D.M. Pedroso, D.J. Williams, L. Li

School of Civil Engineering, The University of Queensland, Brisbane QLD 4072, Australia

## ARTICLE INFO

### Article history:

Received 25 March 2011

Received in revised form 22 August 2011

Accepted 5 October 2011

Available online 10 October 2011

### Keywords:

Molecular dynamics

Bonding models

Fragmentation

## ABSTRACT

The paper presents an extension to the spheropolyhedra method for the simulation of granular materials comprising particles of general shapes with bonding. A bonding, cement, or cohesion model for particles sharing common faces is introduced. The bonding force is elastic and has a strain-based breaking threshold for modelling fracture. An initial study is conducted based on the Brazilian tensile test to check how the parameters of the proposed model affect the principal variables measured in this test. Afterwards, solid cubic blocks are then subjected to a triaxial test to explore the mathematical macroscopic failure model. It is found that the peak strength envelope is the product of the superposition of frictional and fracture failure mechanisms. The fracture failure is mainly produced by an avalanche of broken cohesive bonds. The intensity of the avalanche exhibits a power law distribution, as reported in previous studies. The method allows for random divisions of solid bodies without any pre-existing internal voids. It offers a natural, effective tool to model, simulate and study fragmentation processes in 3D.

© 2011 Elsevier B.V. All rights reserved.

## 1. Introduction

Fragmentation processes have important applications in many fields, including civil and mining engineering, and powder technology. There are innumerable unresolved problems related to fragmentation phenomenon; for example, how to reduce the energy required to obtain a desired rock fragment size or how to minimise the amount of powder resulting by blasting.

One simple approach applied to the study of fragmentation processes is to consider clusters of particles joined by bonding or cohesive forces. These cohesive forces may have many different physical origins, but their effect is the same: opposing the relative displacement between particles, up to a certain threshold value. Examples of these kinds of cohesive forces are mineral cementation, capillarity forces present in unsaturated soils, and van der Waals forces for fine particles like clays.

Models developed to describe fragmentation tend to be very specific to the problems under investigation. Fractures and comminution have been studied by means of statistical models [1], FEM based models [2] and models using the Discrete Element Method (DEM) [3,4].

Discrete element-based models have some advantages over continuum-based models, mainly because the fracture propagation is discrete in nature. In some FEM schemes, the initial point of the

fracture must be artificially introduced, and subsequently the propagation is simulated. In contrast, the initiation crack point in DEM simulations is defined by the broken bonds between the discrete particles, without any external intervention. Moreover, the DEM simulation allows the relationship between the local force thresholds and the macroscopic strength parameters of the sample to be explored.

Most DEM codes are built in 2D, with polygons representing the grains. In codes with discs or spheres, bonding is modelled as a set of *beams* joining the particles with strain thresholds to model the breaking process. In 2D polygonal particles have been used to model cohesive assemblies [5,3,6,7]. However, in 3D the spherical element is still predominantly used [8,4,9–14]. Representing solid bodies as clusters of bounded spheres has drawbacks due to the voids that are present in every packing of spherical particles, regardless of their diameter distribution. Therefore the porosity  $n$  becomes another parameter to be fitted with experimental data [15]. Moreover, the force model for bounded spheres requires the definition of a small boundary value problem, including the mechanical behaviour of “microscopic” beams under bending and torsion, mainly to prevent relative rotations and introduce artificially the effect of particle shape. Polyhedra, and in particular Voronoi mesh based DEM models, have been used before [16] to model fracture. These models however depend heavily on the mesh, declaring stiffness matrices to calculate the force on the mesh nodes just like in FEM methods used for elasticity. Once the mesh is destroyed by the fracture, the interaction between fragments is ignored. In reality, even if the bonding force ceases to exist, the fragments can interact by means of elastic and friction forces which are not

\* Corresponding author.

E-mail addresses: [s.galindotorres@uq.edu.au](mailto:s.galindotorres@uq.edu.au) (S.A. Galindo-Torres), [d.pedroso@uq.edu.au](mailto:d.pedroso@uq.edu.au) (D.M. Pedroso).

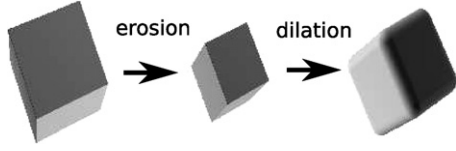


**Fig. 1.** A 3D sphero-cube: Initially the cube is eroded or shrunk by a distance equal to the sphere radius, and then is dilated by the same sphere. After this morphological transformation the cube ends up having rounded corners.

considered in these models. There are also *softer* models for interparticle cohesion to model weaker adhesive forces such as the capillarity interaction [17–19] and the electrostatic adhesion of dry powders [20,21] but these are unsuitable to model rock behaviour and are mostly formulated for spherical elements.

In an earlier study [22], the authors introduced a new way to model particles in 3D using Voronoi-spheropolyhedra tessellations. The present paper, extending this study, introduces a natural and consistent method to simulate bonding between granular particles. Thus fragmentation and fracture processes can fundamentally be investigated. With the proposed model, solid objects with no internal voids can be modelled. Moreover, combined with the Voronoi construction, the strain threshold values have a random distribution and hence are suitable to simulate heterogeneous materials.

This paper is organised as follows: in Section 2 the model is described in detail; followed by a study of the well-known Brazilian Tensile Test [23–25] in Section 3. In Section 4, a detailed study of a solid body response in a True Triaxial Test is presented, followed by some final discussions in Section 5.

## 2. The model

### 2.1. Collision detection

The spheropolyhedra method was initially introduced by Pournin [26] for the simulation of complex-shaped DEM particles. Later, it was modified by Alonso Marroquin [27], who introduced a multi-contact approach in 2D allowing the modelling of non-convex shapes and was extended to 3D by Galindo-Torres et al. [28]. A sphero-polyhedron is a polyhedron that has been eroded and then dilated by a sphere element as seen in Fig. 1. The result is a polyhedron of similar dimensions but with rounded corners.

The best advantage of the spheropolyhedra technique is that it allows for an easy and efficient definition of contact laws between the particles. This is due to the smoothing of the edges of all geometric features by circles (in 2D) or spheres (in 3D).

Regarding the contact between two generic particles  $P_1$  and  $P_2$ , first one has to consider the contact between each geometric feature of particle  $P_1$  with all features of particle  $P_2$ . In mathematical notation, both  $P_1$  and  $P_2$  have a set of vertices  $\{V_{1,2}^i\}$ , edges  $\{E_{1,2}^j\}$ , and faces  $\{F_{1,2}^k\}$ . Thus, a particle is defined as a polyhedron, i.e. a set of vertices, edges and faces, where each one of these geometrical feature is dilated by a sphere.

For simplicity, let's denominate the set of all the geometric features of a particle as  $\{G_{1,2}^i\}$ . Now the function representing this topology can be defined as the distance function for two geometric features according to

$$\text{dist}(G_1^i, G_2^j) = \min(\text{dist}(\vec{X}_i, \vec{X}_j)), \quad (1)$$

where  $\vec{X}_i$  is a 3D vector that belongs to the set  $G_1^i$ . This means that the distance for two geometric features is the minimum Euclidean distance assigned to two points belonging to them.

Since both particles are dilated by their sphero-radii  $R_1$  and  $R_2$ , it can be said that there is a complete contact when the distance between the two geometric features is less than the addition of the corresponding radii used in the sweeping stage, i.e.:

$$\text{dist}(G_1^i, G_2^j) < R_1 + R_2. \quad (2)$$

Here, the advantage of the spheropolyhedra technique becomes evident since this definition is similar to the one for the contact law of two spheres [29].

Now, suppose that the minimum distance for the sets  $G_1$  and  $G_2$  is given by the Euclidean distance between two of their points  $\vec{X}_1$  and  $\vec{X}_2$ . This allows for the definition of a normal vector  $\vec{n}$  given by:

$$\vec{n}(G_1^i, G_2^j) = \frac{\vec{X}_2 - \vec{X}_1}{\|\vec{X}_2 - \vec{X}_1\|}. \quad (3)$$

With this definition, the same expression for the forces defined in conventional DEM codes (for spheres only), can be easily employed in this new method. For example, we can assume a normal elastic force  $\vec{F}_n$  proportional to the overlapping length (see e.g. [29]) defined according to

$$\vec{F}_n(G_1^i, G_2^j) = K_n \delta(G_1^i, G_2^j) \vec{n}(G_1^i, G_2^j), \quad (4)$$

in which  $K_n$  is a parameter called the normal stiffness and

$$\delta = \text{dist}(G_1^i, G_2^j) - R_1 - R_2 \quad (5)$$

is the overlapping distance between the two geometric features.

The previous normal force is defined for a pair of geometric features. The net elastic force is the addition of all these forces for each possible pair of geometric features. However, for general polyhedra, it is only necessary to consider the interactions between vertices and faces and the interaction between edges and edges. The net elastic force is expressed as,

$$\vec{F}_n(P_1, P_2) = \sum_{F_1^i, V_2^j} \vec{F}_n(F_1^i, V_2^j) + \sum_{V_1^i, F_2^j} \vec{F}_n(V_1^i, F_2^j) \quad (6)$$

$$+ \sum_{E_1^i, E_2^j} \vec{F}_n(E_1^i, E_2^j), \quad (7)$$

where only the necessary interactions are included in the summation. Figs. 2(c) and 2(b) illustrate these two types of interactions.

In the spheropolyhedra formalism, a sphere is just a set containing one vertex positioned at the center of the sphere. The sphero-radius is equal to the radius of the sphere and the interaction considers only the vertex–vertex interaction,

$$\vec{F}_n(P_1, P_2) = \vec{F}_n(V_1, V_2),$$

as explained in Fig. 2(a).

Likewise, frictional forces are simply introduced by means of the Cundall–Strack spring method [30], where there is a static friction force given by an incremental tangential displacement  $\vec{\xi}$ , defined according to

$$\vec{F}_t = K_t \vec{\xi} \quad (8)$$

in which  $K_t$  is the tangential stiffness and  $\vec{\xi}$  has an incremental change defined as follows:

$$d\vec{\xi} = \vec{v}_t dt. \quad (9)$$

Here,  $dt$  is the time step and  $\vec{v}_t$  is the component of the relative velocity at the point of contact that is tangential to the normal vector given by Eq. (3). When  $F_t > \mu F_n$ , then the force becomes  $\vec{F}_t = \mu F_n \vec{\xi} / \xi$ . Due to particle rotations,  $\vec{\xi}$  may not be perpendicular to the normal vector at a given time step. To prevent this, at each instant the normal component ( $\vec{n} \cdot \vec{\xi}$ ) is subtracted from it as indicated in previous studies [20]. See Fig. 3.

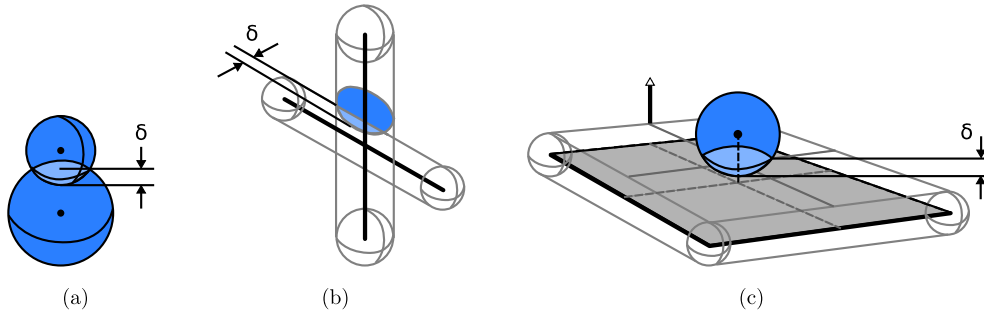


Fig. 2. Definition of the overlapping distance  $\delta$ : (a) vertex–vertex; (b) edge–edge; (c) vertex–face.

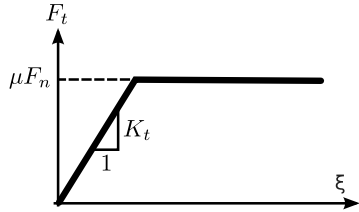


Fig. 3. The value of the tangential force  $F_t$  grows proportionally to the displacement  $\chi$  but when the Coulomb threshold ( $\mu F_n$ ) is reached, it immediately takes this value.

Another (viscous) force is introduced here to account for the proper stability of the simulation. This is defined according to

$$\vec{F}_v = G_n m_e \vec{v}_n + G_t m_e \vec{v}_t \quad (10)$$

in which,  $G_n$  and  $G_t$  are the normal and tangential viscous coefficients, respectively,  $\vec{v}_n$  is the normal component of the relative velocity at the point of contact and  $m_e$  is the effective mass of the particles pair.

Finally, all these forces are added to obtain the net force over a particle. Afterwards, Newton's second law is solved for which here the Verlet algorithm is employed [31]. Each of these forces also provides the torque, where the point of application is at the middle of the line connecting the two contact points for each pair of geometric features that are in contact. With the torque, the angular dynamical equation of movement is solved with the Leap Frog algorithm [28,32].

Recently, the Voronoi construction in 3D was also included into the model in [22], opening the possibility of modelling solid bodies with no internal voids. It is explained briefly in Fig. 4. The advantage of the Voronoi tessellation is the possibility to have random partitions of solids, and therefore, the possibility to run Monte Carlo like simulations for the same set of parameters.

## 2.2. Bonding model

To model bonding, an elastic force is assumed to act between two adjacent spheropolyhedra sharing a common face. The most common force used is the Euler's beam [33]. Hereby we present a simplified model applied for the spheropolyhedra. It can be observed in Fig. 5 the three relative displacements that our model aims to prevent: the normal  $\varepsilon_n$  and tangential  $\varepsilon_t$  strains and the angular displacement along the normal axis  $\theta$ . The expression for the proposed cohesive force in the normal direction is given by:

$$\vec{F}_n = B_n A R(\varepsilon_n) \vec{n}, \quad (11)$$

in which  $B_n$  is the elastic modulus of the material,  $A$  is the shared face area,  $\varepsilon_n$  is the normal strain, and  $\vec{n}$  is the face normal unitary vector. The function  $R(x)$  is the ramp function,

$$R(x) = \begin{cases} x & \text{if } x > 0 \\ 0 & \text{otherwise} \end{cases}, \quad (12)$$

which ensures that this force only opposes tensile deformation. In the case of compression ( $\varepsilon_n < 0$ ), the elastic force of Eq. (6) acts and therefore no action from the cohesive force is needed. With this, the compression modulus  $E_c$  is mostly controlled by the parameter  $K_n$ , as we will show later on, and the tensile modulus  $E_t$  by  $B_n$ . This is an important feature since experimentally both moduli are different [34]. The normal force has exactly the same form as the one used by the beam model [4,33], except that in their case they considered spherical elements and the area  $A$  is not related to any geometrical feature but to the artificial beam. It is also important to mention that this normal force only acts in the case of an extension strain. Tangential displacements may also occur and the bonding force shall deal with them accordingly. Hence, a similar force is introduced for the tangential direction, as follows:

$$\vec{F}_t = B_t A \varepsilon_t \vec{t}, \quad (13)$$

in which  $B_t$  is the tangential elastic modulus, and  $\varepsilon_t$  is the tangential strain in the direction given by the unitary vector tangential to the common face  $\vec{t}$ . Here the ramp function  $R(x)$  is not included since the elastic force (6) does not oppose tangential movement.

Both strains are computed at a common point, which is set at the equilibrium position at the beginning of the simulation. This point is chosen to be the face centroid. Since faces are polygons, each face can be considered to be a plane and the common centroid coordinates on these planes are retained in memory. By the movement and rotation of the faces, the centroid position is different when computed on one face or on the other, and by this relative displacement the strains are obtained.

With spherical elements [4,3,35], torques are also included to prevent the relative rolling of the particles. In the present model, this is not needed, since the real geometry of particles will naturally force the resistance due to rotations. Any relative rotation along an axis perpendicular to the normal vector will be repelled by the elastic collision force. The only torque  $\vec{\tau}$  that needs to be considered is the one opposing rotations in the normal direction, as follows:

$$\vec{\tau} = B_m A \theta \vec{n}, \quad (14)$$

in which  $B_m$  is a modulus representing the resistance to rotation, and  $\theta$  is the angular displacement in the normal direction which can be easily computed from the relative positions of the vertices of each face. Although this torque is needed for the completeness of the model – since the cohesive interaction must oppose any relative movement along all the possible degrees of freedom – we have observed that in most cases is not necessary and can be turned off. In the case illustrated in Fig. 5 this torque is needed since there is no entity opposing the relative rotation of the cubes. But in other configuration such as the Voronoi packing, the DEM

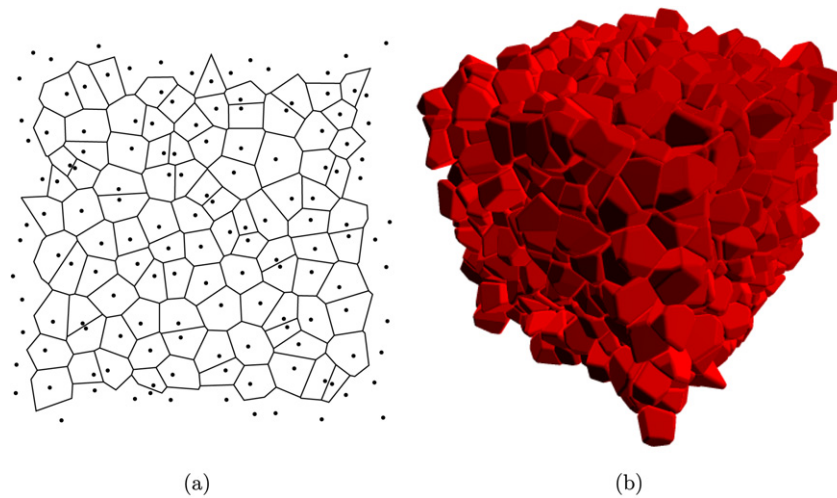


**Fig. 4.** The Voronoi construction explained. (a) The points are randomly distributed in the space and then their corresponding Voronoi polygons (polyhedra) are built by bisecting the joining lines between the given points and its closer neighbours until a convex and closed polygon is obtained. (b) The Voronoi concept extended to 3D.

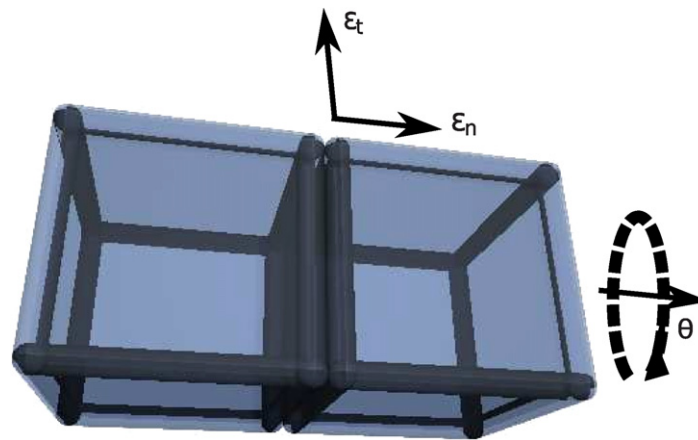


**Fig. 5.** Two spherocubes joined together by a flexible joint representing a bonding or cohesive interaction between them. The bonding force has two components for the normal and tangential directions to the common face. When the two spherocubes rotate and the faces' normal vectors are not longer aligned, the mean normal direction is considered for the force calculation.  $\varepsilon_n$  and  $\varepsilon_t$  are the normal and tangential strains and  $\theta$  is the angle of relative rotation along the normal axis.

particles are closely packed together and they are in contact with several other particles simultaneously. This other particles prevent this undesirable relative rotation by means of the elastic and cohesive forces.

To model fracture, these forces must have a validity range, a threshold value after which they cease to exist. In the present case, all strains are added into one single quantity to be compared with the fixed threshold value  $\varepsilon_{th}$  for the longitudinal strains and an angular threshold  $\theta_{th}$  for  $\theta$ , leading to the following.

$$\text{de-bonding condition: } \frac{|\varepsilon_n| + |\varepsilon_t|}{\varepsilon_{th}} + \frac{|\theta|}{\theta_{th}} > 1, \quad (15)$$

which is a modified version of the von Mises yield criterion commonly used in the beam model [36,43,7,35].

### 3. Brazilian tensile test

#### 3.1. Simulation set-up

One common test used to measure the tensile strength of brittle materials is the Brazilian tensile test [23], in which a disc sample is compressed along an axis parallel to its diameter, inducing a tensile strain perpendicular to it. This tensile behaviour eventually produces a fracture along the compression axis. In Fig. 6(a) the original configuration of the sample is shown and in Table 1,

a summary of the adopted set of parameters for most of the simulations of this paper is given.

The sample is built from an original 2D triangular mesh of a circle. The circle is then extruded in the direction perpendicular to its plane in order to produce a cylinder divided into prism elements. After the compression, shown in Fig. 6(b), the sample will exhibit a vertical fracture, as reported in the literature [38], including also the V-shaped damage zones at the points of contact.

#### 3.2. Failure and elastic properties

The simulated force exerted on the loading plates is shown in Fig. 7. Initially, before failure, the force grows linearly with compression, as an elastic material would behave. It reaches a peak  $F_{max}$  value at about 1.8% strain, and then suddenly drops to zero, showing an abrupt transition to failure. This abrupt decrease in the force is well known in this fundamental test [39]. In most experiments, despite the damage V-shape zones, a point contact is assumed between the plates and the disk and the tensile strength  $\sigma_t$  can be obtained from  $F_{max}$ , the disk diameter  $D$  and thickness  $T$  [34]:

$$\sigma_t = \frac{2F_{max}}{\pi DT}. \quad (16)$$

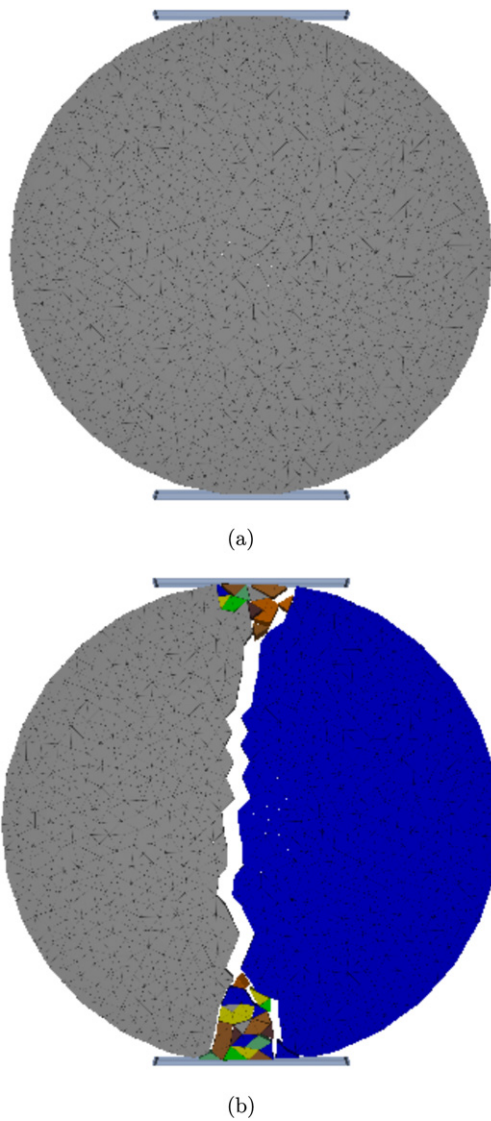


**Fig. 6.** 3D Brazilian disc. (a) The disc is an extrusion of a 2D mesh in the direction perpendicular to the paper resulting into 1544 prism elements. (b) Disk after compression on the verge of collapse.

**Table 1**  
Set of parameters used in the simulations.

Parameter	Value	Unit
$K_n$	$1.0 \times 10^8$	N/m
$K_t$	$1.0 \times 10^8$	N/m
$G_n$	$2.5298 \times 10^3$	1/s
$G_t$	0.0	1/s
$\mu$	0.3	
$B_n$	20.0	GPa
$B_t$	20.0	GPa
$B_m$	3.3	GPa
$\Delta t$	$1.5812 \times 10^{-7}$	s
$\varepsilon_{th}$	0.02	
$\theta_{th}$	0.05	rad
$\Delta h^a$	1	cm

<sup>a</sup> Grid size in Voronoi tessellation.

Tensile strength is an intensive quantity and therefore it should only depend on the bonding, elastic and threshold parameters. Our construction (a 2D mesh extruded into 3D) guaranties that  $B_m$  and  $\theta_{th}$  do not affect the value of  $\sigma_t$  for this particular test. In Fig. 8 the tensile strength is shown for 5 dimensional parameters  $B_n/B_n^r$ ,  $B_t/B_t^r$ ,  $K_n/K_n^r$ ,  $K_t/K_t^r$  and  $\varepsilon_{th}$  where the superscript  $r$  refers to

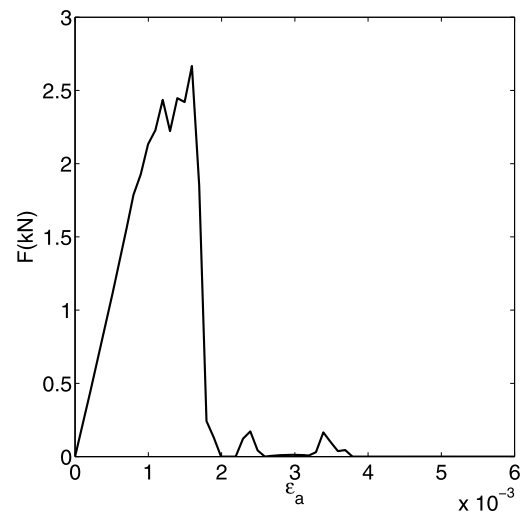


**Fig. 7.** Force exerted on the loading plates as a function of axial strain  $\varepsilon_a$ .

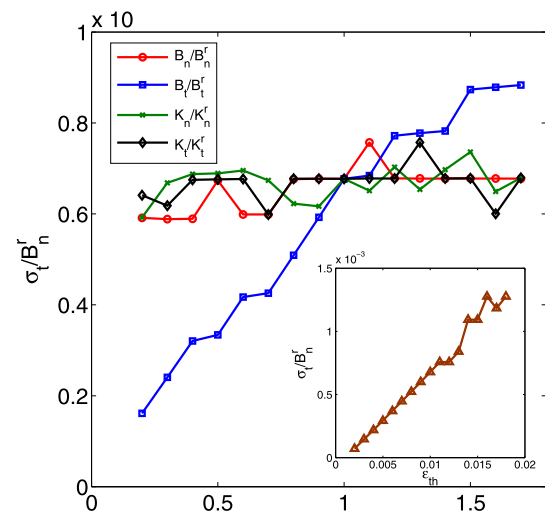


**Fig. 8.** Tensile strength as a function of 4 dimensional parameters and the critical threshold  $\varepsilon_{th}$  (inset).

the reference value given in Table 1. As can be seen, the tensile strength depends mainly on both  $B_t$  and  $\varepsilon_{th}$ , and hence the tensile fracture is due to tangential displacements at the microscopic level.

Another important quantity is the primary slope of the force evolution (Fig. 7) before it reaches  $F_{max}$ . This slope can be used to indirectly measure  $E_c$  [34]. Hence it is an important variable to be tuned by the elastic and cohesive constants. We define this slope as:

$$S = \frac{2.0F(\varepsilon_{max}/2.0)}{\varepsilon_{max}T}, \quad (17)$$

where  $\varepsilon_{max}$  is the strain at which the force is the maximum force. Hence we are computing this slope at the middle point between the origin and the maximum force to ignore the noise introduced by the fracture. Fig. 9 shows the dependence of  $S$  on the elastic and cohesive parameters.  $S$  can be mostly controlled by  $K_n$  with a significant influence of  $B_t$  which can be tuned down for large values of the ratio  $B_t/B_n$ .

It is useful at this point to invoke Buckingham  $\Pi$  theorem [40] and conclude that this intensive quantities ( $\sigma_t$  and  $S$ ) are a function of just 3 adimensional parameters:  $K_n/K_t$ ,  $B_n/B_t$  and  $\varepsilon_{th}$ . The adimensional forms of these functions are:

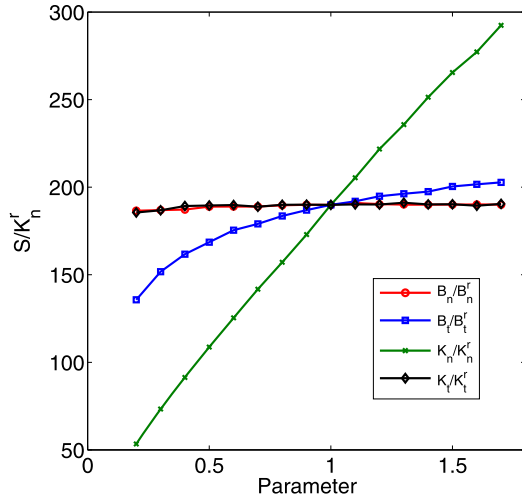


Fig. 9. Slope  $S$  versus the 4 adimensional parameters.

$$\frac{\sigma_t}{B_n} = \Phi_{\sigma_t} \left( \frac{B_n}{B_t}, \varepsilon_{th} \right), \quad (18)$$

$$\frac{S}{K_n} = \Phi_S \left( \frac{K_n}{K_t}, \frac{B_n}{B_t} \right). \quad (19)$$

Although we do not have the analytical form of these functions, their behaviour is shown in Figs. 8 and 9 which can be used as calibration curves. Hence a suitable strategy to calibrate the simulation with experimental data is to first chose a value for  $K_n$  in order to ensure that  $S/K_n$  lies in the range shown in Fig. 9. Afterwards, the values of  $F_{max}$  and  $\varepsilon_{max}$  can be tuned with  $B_n/B_t$  and  $\varepsilon_{th}$ . Any variation induced in  $S$  by changing  $B_n/B_t$  can be corrected by changing  $K_n/K_t$  again. This calibration method has been used before in 2D [6] and sphere based simulations in 3D [15] with excellent results. One advantage of our method is that in sphere based simulations there is a fourth parameter to be considered: the porosity  $n$  [15] which affects the strength and elastic properties. This is unnecessary in the presented model since for all purposes the porosity is zero thanks to the arbitrary shape of the grains.

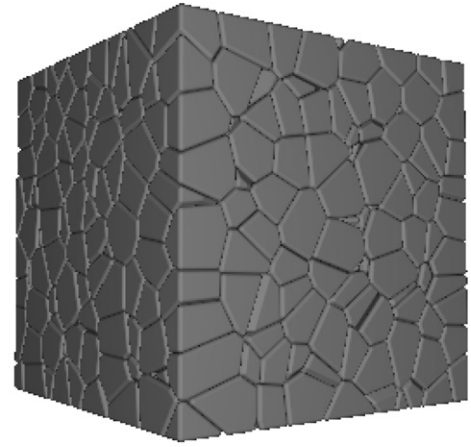
#### 4. True triaxial test

##### 4.1. The set up

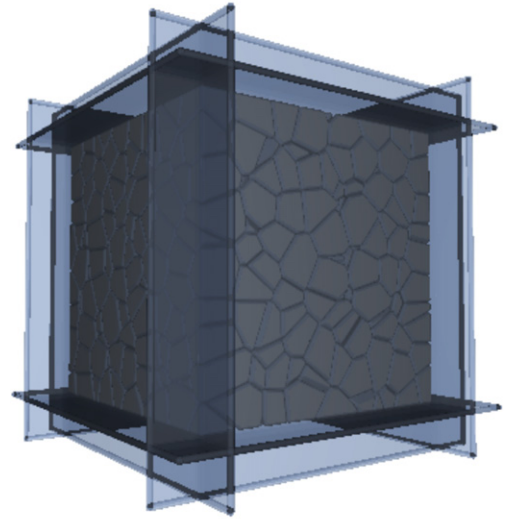
The True Triaxial Test (TTT) is useful to determine the macroscopic failure model of bonded, cohesive, or cohesionless granular materials [41–46]. The 2D version, the biaxial test, has been used as a virtual set up to explore the strength and elastic properties of assemblies of polygonal particles [47–60] and also for 3D assemblies of particles with general shape [61–69].

In Fig. 10, the DEM model setup used in this research is shown, in which the solid sample is enclosed by six square walls. The sample is made of a random array of 1000 Voronoi spheropolyhedra, as explained in [22]. The Voronoi construction ensures a perfect division of the solid with no internal voids. Moreover, each pair of polyhedra produced by this method shares a common planar face allowing the proposed bonding model to be easily implemented. Finally the construction of the Voronoi array is random, so that several samples can be simulated for the same parameter values, in order to obtain expected values and estimations on the measurement errors.

Some important quantities commonly used to analyse the results of true triaxial tests are defined as follows: the mean ( $p$ ) and deviatoric ( $q$ ) stress invariants, and the volumetric ( $\varepsilon_v$ ) and deviatoric ( $\varepsilon_d$ ), strains as defined by:



(a)



(b)

Fig. 10. (a) Cohesive block divided into an array of 1000 Voronoi spheropolyhedra. (b) The same block inside the True Triaxial Test set up.

$$p = \frac{\sigma_1 + \sigma_2 + \sigma_3}{3}, \quad (20)$$

$$q = \sqrt{\frac{(\sigma_1 - \sigma_2)^2 + (\sigma_1 - \sigma_3)^2 + (\sigma_2 - \sigma_3)^2}{2}}, \quad (21)$$

$$\varepsilon_v = \varepsilon_1 + \varepsilon_2 + \varepsilon_3, \quad (22)$$

$$\varepsilon_d = \sqrt{\frac{2}{3}((\varepsilon_1 - \varepsilon_2)^2 + (\varepsilon_1 - \varepsilon_3)^2 + (\varepsilon_2 - \varepsilon_3)^2)} \quad (23)$$

in which  $\sigma_i$  are the principal stress invariants, and  $\varepsilon_i$  are the principal strain invariants. Extension strains are taken as positive.

##### 4.2. Elastic properties

The TTT offers another possibility to measure the elastic properties of the simulated material before doing fracture simulations. With a simple compression test, the Poisson ratio  $\nu$  and compression modulus  $E_c$  can be measured by applying a constant strain rate along the 3 axis and a zero pressure along the other two directions to represent and unconfined test. By measuring the strains in the 1 and 2 directions we have,

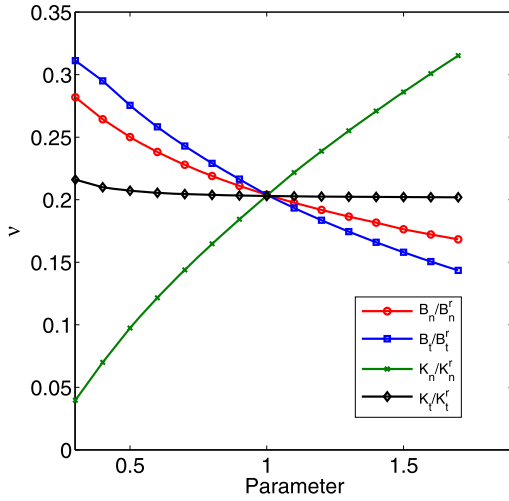


Fig. 11. Poisson ratio  $\nu$  versus the 4 adimensional parameters.

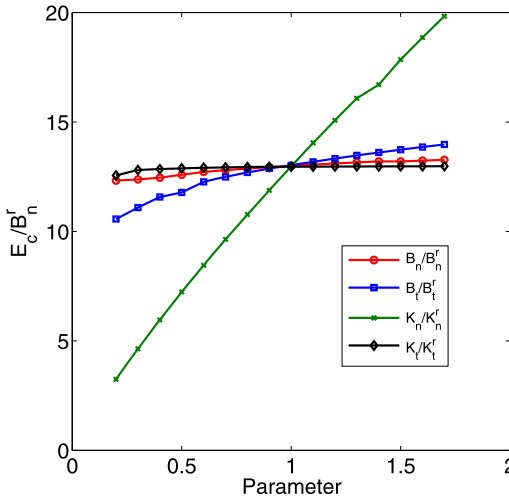


Fig. 12. Compressive modulus  $E_c$  versus the 4 adimensional parameters.

$$\nu = -\frac{\varepsilon_1 + \varepsilon_2}{2\varepsilon_3}, \quad (24)$$

where the numerator has been divided by 2 to account for possible differences between  $\varepsilon_1$  and  $\varepsilon_2$ . For perfect isotropic samples the two strains should be equal, but the Voronoi construction introduces imperfections that need to be considered. Fig. 11 shows how  $\nu$  depends on the elastic and cohesive parameters. It is a complex function of  $K_n$ ,  $B_n$  and  $B_t$  with practically no effect from  $K_t$ . For small values of  $K_n$ ,  $\nu$  is small. Again this is an effect from the ramp function of Eq. (11). In contrast, it does decrease with the bounding constants. As the bounding contacts become stiffer, it is more difficult to produce the Poisson's effect.

With the same test, the compressive modulus,

$$E_c = \frac{\sigma_3}{\varepsilon_3} \quad (25)$$

can be measured. Fig. 12 shows that  $K_n$  strongly affects  $E_c$  just as it also affects  $S$  for the Brazilian test.  $E_c$  is also changed by  $B_t$  mainly due to the sliding of the Voronoi polyhedra along the common faces during the compression test.

On the other hand, Fig. 13 shows the tensile modulus  $E_t$ . It is measured with the same TIT set up but now a positive strain rate is applied. To ensure the sample is being pulled apart, the walls are attached to the grains in contact with the them with the same cohesive normal force of Eq. (11) but with no tangential forces. As

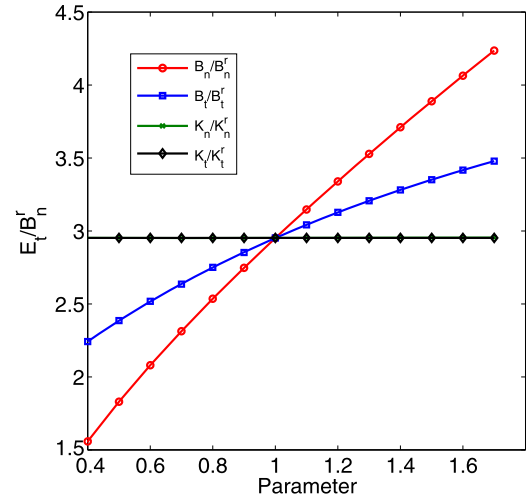


Fig. 13. Tensile modulus  $E_t$  versus the 4 adimensional parameters.

can be seen the elastic constants  $K_n$  and  $K_t$  do not affect  $E_t$ , it is only affected by the cohesive constants. This is expected since when the sample is subjected to extensive stresses, the individual grains are separated from each other and Eq. (6) does not apply.

In a similar way as we did for the Brazilian test, it can be said that

$$\frac{E_c}{B_n} = \Phi_{E_c} \left( \frac{K_n}{K_t}, \frac{B_n}{B_t} \right), \quad (26)$$

$$\frac{E_t}{B_n} = \Phi_{E_t} \left( \frac{B_n}{B_t} \right), \quad (27)$$

$$\nu = \Phi_\nu \left( \frac{K_n}{K_t}, \frac{B_n}{B_t} \right). \quad (28)$$

Again Figs. 11, 12 and 13 can be used for calibration by initially choosing a value for  $B_n$  to ensure that  $E_c/B_n$  lies in the range of Fig. 12 and then tune  $\nu$  with the cohesive constants. Any alteration to  $E_c$  can be corrected solely by  $K_n/K_t$ .  $E_t$  is easier to fit since it only depends on  $B_n/B_t$ . The dependence on  $B_t$  can also be explained by the fact that in the Voronoi construction some particles will slide against each other when the sample is extended and then Eq. (13) applies. If the Voronoi mesh is changed by a uniform mesh of cubes, there would be no tangential sliding and therefore  $E_t = B_n$  and  $\nu = 0$ . This dependence of the elastic properties on the constitutive mesh demands further study.

As a final step to validate the method to measure the elastic properties, a cantilever beam was simulated as shown in Fig. 14. It was built from a mesh of 1250 Voronoi spheropolyhedra. The dimensions are a length of  $L = 50$  cm and a square cross section of side  $s = 5$  cm. The elastic and cohesive parameters are  $K_n = K_t = 5.0 \times 10^8$  N/m and  $B_n = B_t = 200$  GPa which produces  $E_c = 674$  GPa. At each boundary there is a plate similar to the ones used for the Brazilian test simulations. The left plate is fixed and there is a force  $F = 6.0 \times 10^4$  N applied in the right plate center.

By keeping  $s$  small, Euler's beam theory [70] can be used to determine the deviation  $w$  of the cantilever's middle plane along the  $x$  coordinate as:

$$w(x) = \frac{Fx^2(3L - x)}{6E_c I}, \quad (29)$$

where  $I = s^4/12$  is the second area moment [70] of the square cross section. To find the middle plane of the Voronoi cantilever, at the beginning of the simulation each particle vertex was checked and the ones close to this plane (by a distance of  $0.05L$ ) were tagged. At the end of the simulation, the tagged vertices' vertical

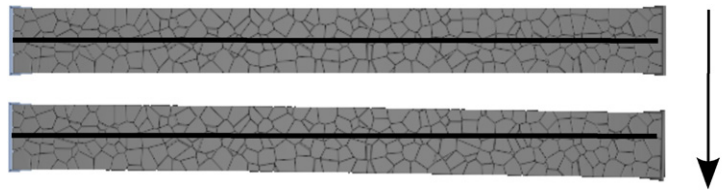


Fig. 14. A cantilever simulated by a 1250 Voronoi spheropolyhedra mesh limited by two vertical plates and with a force  $F$  applied to the right one.

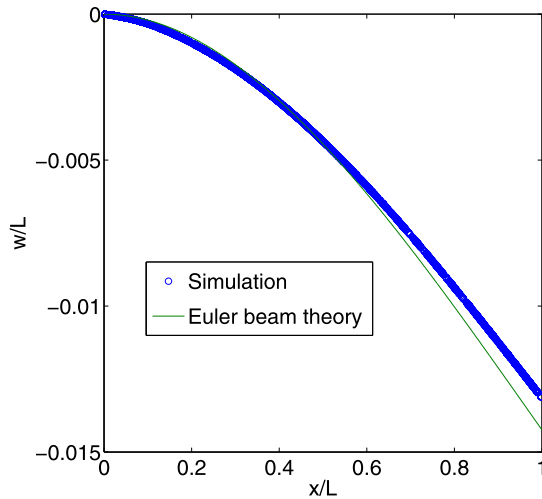


Fig. 15. Deflection of the cantilever middle plane obtained from the DEM simulation and compared with Eq. (29).

displacement is recorded. The results are shown in Fig. 15 and a fair agreement between Euler's theory and the DEM simulation is found.

#### 4.3. Stress paths

The stress path applied in the following TTT simulations in order to "break" the sample is the  $p$ -constant path number (2) as sketched in Fig. 16. In this case, the breakage will occur due to a deviation of one or more stress components with respect to each other. This deviation is measured by an increase of the  $q$  invariant. Nonetheless, to initialise the system in a fairly stable condition, an isotropic loading (path number (1) in Fig. 16) is first applied. Thus, the testing has two stages: (1) isotropic compression with  $\sigma_1 = \sigma_2 = \sigma_3$ ; and (2) application of a constant strain rate along the  $z$ -direction, compressing the sample, in which  $\sigma_3$  will increase. To keep  $p$  constant,  $\sigma_1$  and  $\sigma_2$  will have to decrease.

Achieving a  $p$ -constant path is relatively easy with a strain-controlled path. The walls perpendicular to the  $z$ -axis are moved with constant velocity and the force exerted on these walls by the sample is used to compute the vertical stress  $\sigma_3$ . The stresses  $\sigma_1$  and  $\sigma_2$  are determined by considering the constant pressure constraint. However, there is an important exception to be considered: if the applied pressure  $p$  is small, there may be cases in which  $\sigma_3$  is also small enough to result in positive (tension) values for  $\sigma_1$  and  $\sigma_2$ , meaning that eventually the vertical planes will lose contact with the sample. This is an undesirable, but natural, effect for the current study. In order to avoid this problem, the particles in contact with the walls are attached to them. They are subjected to the same normal cohesive force given by Eq. (11), but not including the tangential force nor the restitution torque. Also, the breaking threshold is suppressed for these special joints (walls-particles). Hence, when the horizontal stresses are positive they actually are pulling the sample apart.

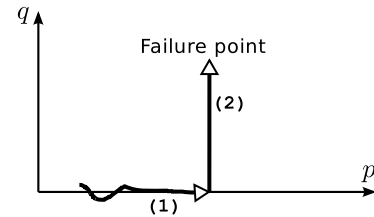


Fig. 16. Stress paths applied in the DEM simulation of a true triaxial test.

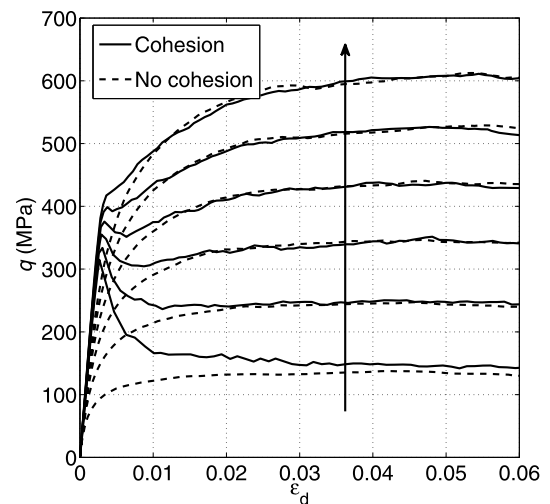


Fig. 17. Simulated behaviour during the loading path number (2) (shearing). The vertical arrow indicates the direction of confining pressure increase. The 6 values for  $p$  are: 110, 130, 150, 170, 190 and 210 MPa.

#### 4.4. Preliminary results

Simulations with different initial pressures are carried out. The results are shown in Fig. 17. Cases with and without cohesion are investigated. Where cohesion is present, for low pressures the sample behaves like a brittle material. It has a peak value for  $q$  and it then goes to a residual state. The peak value is preceded by a linear increment typical of an elastic material. The peak stress is almost unnoticeable at high pressures, being overtaken by the frictional residual state. Indeed, by observing the sample without cohesion the residual state can be described entirely by a frictional failure.

It is well known that, for a purely frictional cohesionless material, the mathematical representation (failure model) that best fits the observed data will be a straight line in the  $p$ - $q$  plane. This is why this residual stress value grows as the pressure increases. The peak stress is related to both the frictional and cohesive thresholds. In Fig. 18, the peak stress is shown for two different breaking strain values  $\epsilon_{th}$  (see Eq. (15)) for the individual particle pairs. The results demonstrate that the peak stress value is strongly related to the cohesive breaking point as expected. Indeed a higher microscopic strain threshold allows the sample to be deformed to a higher degree before reaching the cohesive failure. This results agrees with the previous measurement of the tensile strength  $\sigma_t$

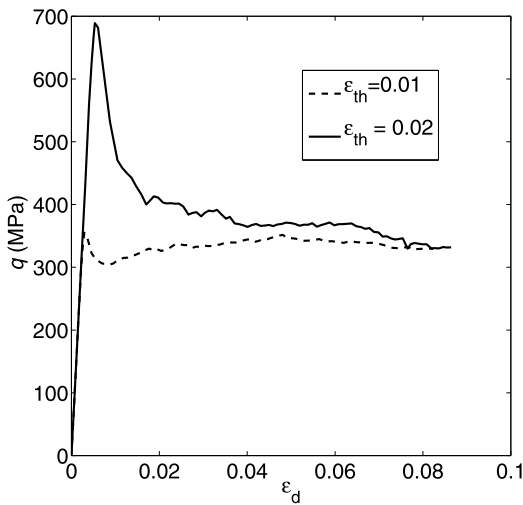


Fig. 18. Simulated behaviour, during shearing, with two different threshold values  $\varepsilon_{th}$ .

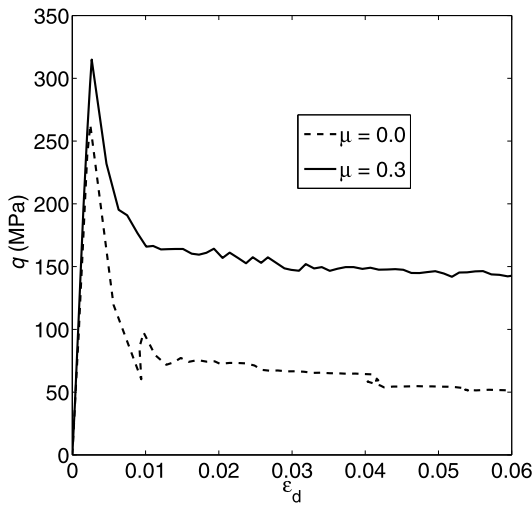


Fig. 19. Simulated behaviour, during shearing, with two different friction coefficients  $\mu$ .

mentioned before in the Brazilian test simulation (see Fig. 8). However, it also depends on the friction angle, as shown in Fig. 19. It can be concluded that there is a superposition of two different failure processes: (1) de-bonding or de-cohesion – characterised by the breaking threshold strain  $\varepsilon_{th}$  –; and (2) sliding (frictional failure) – characterised by the friction coefficient  $\mu$  –, both affecting the peak stress. This superposition of effects has also been found in disc-based DEM simulations [71]. This will be studied in detail in the following section when the failure surface is obtained.

The predicted macroscopic volumetric behaviour resembles the one a brittle material would exhibit. As seen in Fig. 20, initially there is only compression on the sample for both the cohesive and cohesionless samples. However, while the cohesionless sample quickly starts dilating, the cohesive sample only expands once it reaches the peak stress. Afterwards, they both show similar dilatancy angles. The dilatancy is expected to be similar for both cases since it is related to the residual state, which in turn is related to the friction coefficient [71]. It is important to mention that although in Fig. 18  $q$  reaches a saturation value, this is not necessary related to a value of zero for the dilatancy angle as has been observed in triaxial test simulations of loose soils [29]. This indicates that after an important portion of the bounding contacts are bro-

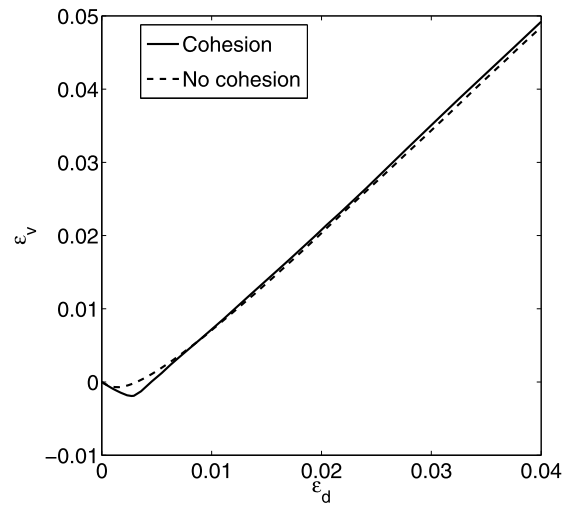


Fig. 20. Obtained dilatancy behaviour.

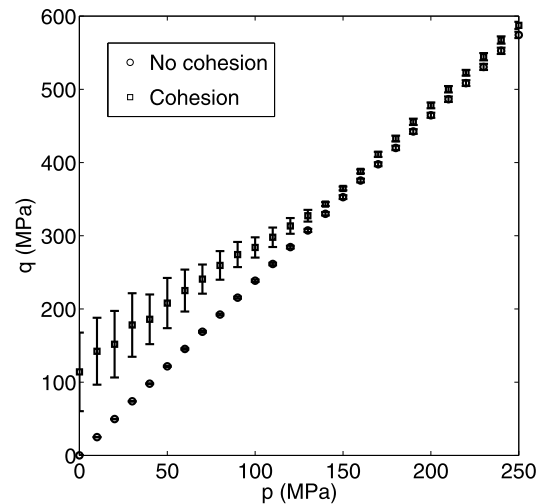


Fig. 21. Failure envelope for the peak stress for both: bonded and de-bonded samples.

ken, the sample behaves like a loose granular assembly with the grains formed by small clusters of particles that are still attached to each other.

#### 4.5. Failure surface

Applying the  $p$ -constant path described earlier, the macroscopic failure model can be investigated. This model is represented by a surface in the stress tensor space or by a curve in the space of stress invariants  $p$  and  $q$  – the so-called failure envelope. For each confining pressure, eight different random simulations were undertaken in order to find the shape of the curves of an eventual failure model with the average value obtained with these realisations.

In Fig. 21, the average results are shown as well as the standard deviation representing by error bars. Analogously as observed in Fig. 17, the bonding effect on the peak stress is superseded by the frictional failure point. After a given pressure (approximately 140 MPa) the failure envelope becomes reasonably linear. Except for the initial (peak) vertical shift, it has the same slope as the non-cohesive failure envelope. This initial part of the envelope, representing higher strength, is due mainly due to the bonding effect. By observing Figs. 18, 19, 20 and 21 we may conclude that after the breakage of most of the bonds, the sample becomes a loose granular assembly enclosed in the TTT set-up. This is the

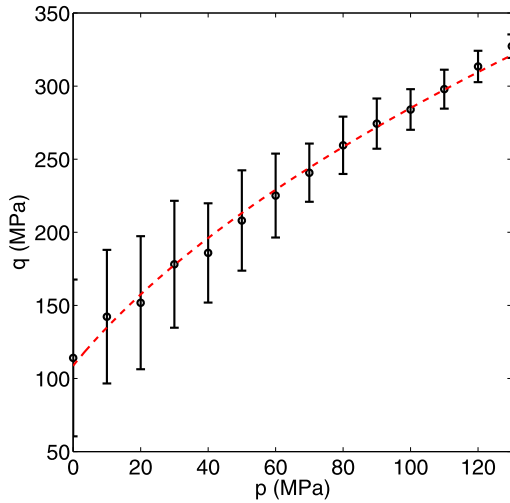


**Fig. 22.** Peak strength envelope fitted with the Hoek–Brown model. Fitting parameters are  $A = 203.3 \pm 10.1$  MPa and  $B = 69.3 \pm 2.6$  MPa and the correlation factor is  $R^2 = 0.9944$ .

reason that at the end, for high enough pressures, the failure envelope is mainly frictional.

The results also show a peak strength even for the case of zero confining pressure. In this case, the walls are barely touching the sample, but still some work needs to be done in order to break the bonds. This work comes from the shearing processes producing a non-zero peak strength even for the unconfined test. This, as well as the curve shape of the peak strength envelope, is a common feature, usually observed in rocks [72].

The empirical failure criterion model of Hoek–Brown [73] is commonly used to describe the shape of the peak strength envelope. This criterion is usually expressed in terms of the maximum principal stress  $\sigma_1$  and the minimum one  $\sigma_3$  at failure, as follows:

$$\sigma_1 = \sigma_3 + \sqrt{A\sigma_3 + B^2}, \quad (30)$$

in which  $A$  and  $B$  are the fitting parameters, with pressure dimensions. Expressed in terms of the pressure and deviatoric stresses this relation becomes:

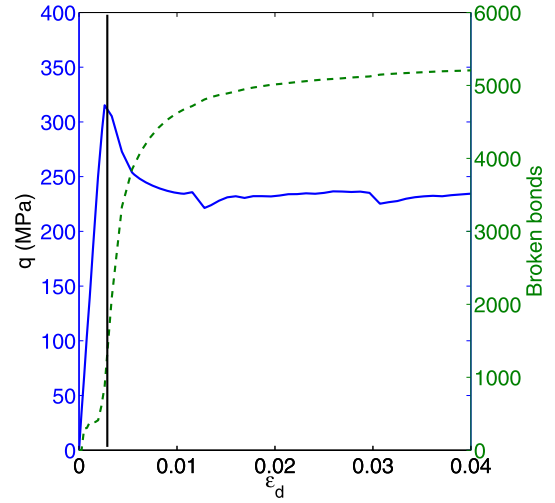
$$q = \frac{1}{6}(\sqrt{A^2 + 36Ap + 36B^2} - A). \quad (31)$$

Fig. 22 shows the results of the fitting of the Hoek–Brown model to the subset of data corresponding to the peak strength envelope of Fig. 21.

#### 4.6. Burst statistics

As outlined in the literature [1], burst avalanches play an important role in characterising fracture-failure phenomena. When one element on the ensemble fails, suddenly the stress is redistributed among the remaining elements, causing further failures. If several elements fail simultaneously, a macroscopic failure is detected by this avalanche effect. Experimentally, it has been shown that this micro-fracture process can be measured by the acoustic emissions they produce [74] and that the distribution of emissions per time interval follows a power law.

In Fig. 23, the correlation between the avalanche of broken bonds and the peak strength is shown. There is an initial increment of broken bonds due to the shearing process, but it reaches a stable value and does not mark the onset of the avalanche effect. A second accelerated increment occurs and this one signals the initiation of macroscopic failure. This phenomenon is consistently



**Fig. 23.** Deviatoric stress  $q$  evolution (left axis, solid line) compared with the bond breaking dynamics (right axis, dashed line). The vertical line marks the origin of the second breaking avalanche related to the peak failure point.

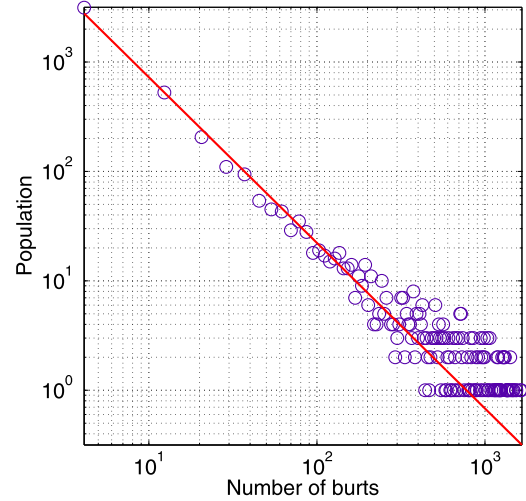


**Fig. 24.** Histogram of number of broken bonds over a given time span in log–log scale. The line represents power law fitting.

found in all the experiments described herein. Once the second stable state is reached, the system enters frictional failure and no more bonds are broken; i.e., the failure is entirely frictional.

It has been reported that the distribution of burst produced over a given time span follows a power law [75,1]. In Fig. 24, the histogram of broken bonds for all the realisations considered is shown. In the present case, the fitted exponent of this (power-law) distribution is  $-1.51 \pm 0.03$ .

To have a random distribution of broken bonds, a random distribution of breaking thresholds is also needed. Eq. (15) ensures a uniformly distributed threshold value among all the bonds if the contact area  $A$  remains the same. By Eqs. (11), (13) and (14) for the same parameters; the only value that is different is the face area  $A$ . In the case of the Voronoi construction, the area of the different spheropolyhedra is also randomly distributed (Fig. 25). This distribution for the area is fitted with a simple spline function. The shape of the obtained distribution function for Voronoi face area is similar to some previously found in Voronoi tessellations of uniform packings of spheres [76].

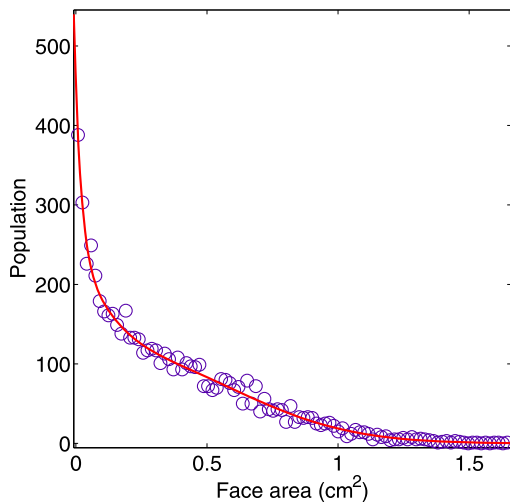


Fig. 25. Histogram of face area for the different bonds considered in the Voronoi construction. The solid line exists for visual aid.

## 5. Conclusions

In this paper, a method to model bonded (or cohesive) granular materials formed by discrete particles of arbitrary shapes has been proposed. The model is the combination of the spheropolyhedra approach to model collision of polyhedral particles with a set of cohesive elements joining particles sharing a common face. In the presented simulations close packings of particles are generated by random meshes such as the Voronoi tessellation.

Simulations with the Brazilian tensile test demonstrate the capabilities of the presented model, which reproduces some typical features observed in this test. In particular, the vertically-orientated crack and the sudden drop in the contact force that indicates the onset of the global failure of the disc are observed. The primary slope and tensile strength can be controlled by the parameters of our model. The tensile strength depends mainly on the fixed strain threshold for breakage as well as the microscopic cohesive constants, while the elastic behaviour given by the primary slope is affected mainly by the contact spring law for collision.

Cubic blocks made of Voronoi particles were simulated in a virtual true triaxial test TTT. With it more elastic properties were observed. We concluded that the compressive modulus depends on the collision law while the tensile modulus depends on the cohesive force. In contrast, Poisson's ratio is a complex function of both elastic and cohesive parameters. After the elastic properties were measured, a cantilever simulation was done to validate our model with the well-known Euler's beam theory of elasticity given a fair agreement between the proposed model and the classical theory. Triaxial test simulations were also carried out to observe the macroscopic mathematical failure envelope. For low pressures, a peak Hoek–Brown strength envelope is observed. As the pressure increases, this envelope becomes the frictional failure envelope. It has also been found that the peak strength is made up by superimposed contributions of both frictional and bonding failure phenomena. On the other hand, the residual state is mostly produced purely by the friction effects. This additive nature of peak strength has been reported elsewhere in 2D simulations with disks only [71]. Moreover, the predicted Hoek–Brown failure envelope is commonly found in rocks and over-consolidated clays where the cohesive interactions between particles are strong.

Finally, a relationship between the sudden increment in the number of broken bonds with the initiation of failure has been found. This avalanche effect is usually modelled by a power law distribution, which is supported by the present results. For instance, after sampling all of the realisations considered, a power

law exponent of  $-1.51 \pm 0.03$  was found for the system. It is important to point out that this power law distribution is due to the random distribution of contact areas produced by the Voronoi construction. This area distribution translates into a random distribution of breaking thresholds for the cohesive elements.

In conclusion, the model allows simulations of solid bodies with no internal voids, in contrast to previous studies in which bodies are made of clumps of spheres. The model includes parameters representing the elastic response of the material, as well as breaking thresholds to control its strength. In the series of test presented in this paper, the model has been shown to reproduce many well-known features of failure and damage processes such as the power law distribution of broken elements. The presented examples demonstrate how the model can be used to study complex fragmentation processes in 3D that, so far, have been simulated with spherical clusters only.

## Acknowledgements

We thank F. Alonso-Marroquin for useful discussions. The software used for all the simulations presented in this paper is based on the open source library MechSys (URL: <http://mechsys.nongnu.org/index.shtml>) developed by the authors.

## References

- [1] S. Pradhan, A. Hansen, P.C. Hemmer, Crossover behavior in failure avalanches, *Phys. Rev. E* 74 (1) (2006) 016122, doi:10.1103/PhysRevE.74.016122.
- [2] N. Sukumar, N. Moes, B. Moran, T. Belytschko, Extended finite element method for three-dimensional crack modelling, *Internat. J. Numer. Methods Engrg.* 48 (11) (2000) 1549–1570.
- [3] F. Kun, H.J. Herrmann, A study of fragmentation processes using a discrete element method, *Comput. Methods Appl. Mech. Engrg.* 138 (1996) 3–18.
- [4] H. Carmona, F. Wittel, F. Kun, H. Herrmann, Fragmentation processes in impact of spheres, *Phys. Rev. E* 77 (5) (2008) 51302.
- [5] G. D'Addetta, F. Kun, E. Ramm, On the application of a discrete model to the fracture process of cohesive granular materials, *Granular Matter* 4 (2) (2002) 77–90.
- [6] A. Fakhimi, T. Villegas, Application of dimensional analysis in calibration of a discrete element model for rock deformation and fracture, *Rock Mech. Rock Engrg.* 40 (2) (2007) 193–211.
- [7] S. Galindo-Torres, J. Muñoz Castaño, Simulation of the hydraulic fracture process in two dimensions using a discrete element method, *Phys. Rev. E, Statist. Nonlin. Soft Matter Phys.* 75 (6).
- [8] Y. Wang, P. Mora, Modeling wing crack extension: Implications for the ingredients of DEM, *Pure Appl. Geophys.* 165 (3) (2008) 609–620.
- [9] S. Antonyuk, M. Khanal, J. Tomas, S. Heinrich, L. Morl, Impact breakage of spherical granules: Experimental study and DEM simulation, *Chem. Eng. Process.* 45 (10) (2006) 838–856.
- [10] W. Schubert, M. Khanal, J. Tomas, Impact crushing of particle–particle compounds – experiment and simulation, *Internat. J. Mineral Process.* 75 (1–2) (2005) 41–52.
- [11] M. Khanal, W. Schubert, J. Tomas, Dem simulation of diametrical compression test on particle compounds, *Granular Matter* 7 (2) (2005) 83–90.
- [12] A. Hassanpour, S. Antony, M. Ghadiri, Effect of size ratio on the behaviour of agglomerates embedded in a bed of particles subjected to shearing: DEM analysis, *Chem. Eng. Sci.* 62 (4) (2007) 935–942.
- [13] D. Potyondy, P. Cundall, A bonded-particle model for rock, *Int. J. Rock Mech. Min. Sci.* 41 (8) (2004) 1329–1364.
- [14] H. Péron, J. Delenne, L. Laloui, M. El Yousoufi, Discrete element modelling of drying shrinkage and cracking of soils, *Comput. Geotech.* 36 (1–2) (2009) 61–69.
- [15] J. Rojek, E. Oñate, C. Labra, H. Kargl, Discrete element modelling of rock cutting, in: *Particle-Based Methods*, Springer, Netherlands, 2011, pp. 247–267.
- [16] A. Delaplace, R. Desmorat, Discrete 3D model as complimentary numerical testing for anisotropic damage, *Internat. J. Fract.* 148 (2) (2007) 115–128.
- [17] F. Soulié, F. Cherblanc, M. El Yousoufi, C. Saix, Influence of liquid bridges on the mechanical behaviour of polydisperse granular materials, *Internat. J. Numer. Anal. Meth. Geomech.* 30 (3) (2006) 213–228.
- [18] V. Richefeu, M. El Yousoufi, F. Radjaï, Shear strength properties of wet granular materials, *Phys. Rev. E* 73 (5) (2006) 051304.
- [19] V. Richefeu, M. El Yousoufi, R. Peyroux, F. Radjaï, A model of capillary cohesion for numerical simulations of 3d polydisperse granular media, *Internat. J. Numer. Anal. Meth. Geomech.* 32 (11) (2008) 1365–1383.

- [20] S. Luding, Cohesive, frictional powders: Contact models for tension, *Granular Matter* 10 (4) (2008) 235–246.
- [21] R. Tykhoniuk, J. Tomas, S. Luding, M. Kappl, L. Heim, H. Butt, Ultrafine cohesive powders: From interparticle contacts to continuum behaviour, *Chem. Eng. Sci.* 62 (11) (2007) 2843–2864.
- [22] S. Galindo-Torres, D. Pedroso, Molecular dynamics simulations of complex-shaped particles using Voronoi-based spheropolyhedra, *Phys. Rev. E, Statist. Nonlin. Soft Matter Phys.* 81 (6) (2010) 061303.
- [23] J. Jaeger, E. Hoskins, Rock failure under the confined Brazilian test, *J. Geophys. Res.* 71 (10) (1966) 2651–2659.
- [24] H. Guo, N. Aziz, L. Schmidt, Rock fracture-toughness determination by the Brazilian test, *Engrg. Geol.* 33 (3) (1993) 177–188.
- [25] J. Hudson, Tensile strength and the ring test, *Int. J. Rock Mech. Min. Sci. (Abstracts)* 6 (1969) 91–97.
- [26] L. Pournin, T. Liebling, A generalization of distinct element method to tridimensional particles with complex shapes, in: *Powders & Grains 2005*, Balkema, Leiden, 2005, pp. 1375–1478.
- [27] F. Alonso-Marroquín, Spheropolygons: A new method to simulate conservative and dissipative interactions between 2d complex-shaped rigid bodies, *Europhys. Lett.* 83 (1) (2008) 14001.
- [28] S. Galindo-Torres, F. Alonso-Marroquín, Y. Wang, D. Pedroso, J. Muñoz Castaño, Molecular dynamics simulation of complex particles in three dimensions and the study of friction due to nonconvexity, *Phys. Rev. E* 79 (6) (2009) 060301.
- [29] N. Belheine, J. Plassiard, F. Donzé, A. Darve, F. Seridi, Numerical simulation of drained triaxial test using 3D discrete element modeling, *Comput. Geotech.* 36 (1–2) (2009) 320–331.
- [30] P. Cundall, O. Strack, A discrete numerical model for granular assemblies, 1979.
- [31] L. Verlet, Computer experiments on classical fluids. I. Thermodynamical properties of Lennard-Jones molecules, *Phys. Rev.* 159 (1) (1967) 98–103.
- [32] Y. Wang, S. Abe, S. Latham, P. Mora, Implementation of particle-scale rotation in the 3-D lattice solid model, *Pure Appl. Geophys.* 163 (9) (2006) 1769–1785.
- [33] T. Poeschel, T. Schwager, *Computational Granular Dynamics*, Springer, Berlin, 2004.
- [34] Y. Jianhong, F. Wu, J. Sun, Estimation of the tensile elastic modulus using Brazilian disc by applying diametrically opposed concentrated loads, *Int. J. Rock Mech. Min. Sci.* 46 (3) (2009) 568–576.
- [35] F. Kun, H.J. Herrmann, Transition from damage to fragmentation in collision of solids, *Phys. Rev. E* 59 (3) (1999) 2623–2632.
- [36] B. Behera, F. Kun, S. McNamara, H. Herrmann, Fragmentation of a circular disc by impact on a frictionless plate, *J. Phys.: Condens. Matter* 17 (2005) S2439.
- [37] F. Wittel, F. Kun, H. Herrmann, B. Kroplin, Fragmentation of shells, *Phys. Rev. Lett.* 93 (3) (2004) 35504.
- [38] G. D'Addetta, Discrete models for cohesive frictional materials, Fakultät Bauingenieur- und Umweltingenieurwissenschaften, Universität Stuttgart.
- [39] W. Zhu, C. Tang, Numerical simulation of Brazilian disk rock failure under static and dynamic loading, *Int. J. Rock Mech. Min. Sci.* 43 (2) (2006) 236–252.
- [40] E. Buckingham, On physically similar systems; illustrations of the use of dimensional equations, *Phys. Rev.* 4 (4) (1914) 345–376, doi:10.1103/PhysRev.4.345.
- [41] P.V. Lade, J.M. Duncan, Cubical triaxial tests on cohesionless soil, *J. Soil Mech. Found. Div. (ASCE)* 99 (10) (1973) 793–812.
- [42] H. Matsuoka, T. Nakai, Stress-deformation and strength characteristics of soil under three different principal stresses, in: *Proc. JSCE*, vol. 232, 1974, pp. 59–70.
- [43] E. Fradis, S. Frydman, Stress-strain behaviour of sand under generalized stress conditions, in: *Proc. IX ICSMFE Constitutive Equations of Soils, 1977*, pp. 57–64.
- [44] M. Goldscheider, True triaxial tests on dense sand, in: *Proc. Int. Workshop on Constitutive Relations for Soils, Grenoble, 6–8 Sep. 1982*, pp. 11–54.
- [45] E.Q. Chowdhury, T. Nakai, Consequences of the *tij*-concept and a new modeling approach, *Comput. Geotech.* 23 (1998) 131–164.
- [46] D.M. Pedroso, Mathematical representation of the cyclic mechanical behaviour of saturated and unsaturated soils, PhD thesis, University of Brasília, Brasília, Brasil, 2006 (in Portuguese).
- [47] H.G. Matuttis, S. Luding, H.J. Herrmann, Discrete element simulations of dense packings and heaps made of spherical and non-spherical particles, *Powder Technol.* 109 (1–3) (2000) 278–292, doi:10.1016/S0032-5910(99)00243-0.
- [48] G. D'Addetta, F. Kun, E. Ramm, H. Herrmann, From solids to granulates – discrete element simulations of fracture and fragmentation processes in geomaterials, in: P. Vermeer, H. Herrmann, S. Luding, W. Ehlers, S. Diebels, E. Ramm (Eds.), *Continuous and Discontinuous Modelling of Cohesive-Frictional Materials*, in: *Lecture Notes in Physics*, vol. 568, Springer, Berlin/Heidelberg, 2001, pp. 231–258.
- [49] F. Alonso-Marroquín, Spheropolygons: A new method to simulate conservative and dissipative interactions between 2d complex-shaped rigid bodies, *EPL (Europhys. Lett.)* 83 (1) (2008) 14001, doi:10.1209/0295-5075/83/14001.
- [50] F. Alonso-Marroquín, H.J. Herrmann, Calculation of the incremental stress-strain relation of a polygonal packing, *Phys. Rev. E* 66 (2) (2002) 021301, doi:10.1103/PhysRevE.66.021301.
- [51] F. Alonso-Marroquín, H.J. Herrmann, The incremental response of soils. An investigation using a discrete-element model, *J. Engrg. Math.* 52 (2005) 11–34, doi:10.1007/BF02694028.
- [52] F. Alonso-Marroquín, S. Luding, H.J. Herrmann, I. Vardoulakis, Role of anisotropy in the elastoplastic response of a polygonal packing, *Phys. Rev. E* 71 (5) (2005) 051304, doi:10.1103/PhysRevE.71.051304.
- [53] F. Alonso-Marroquín, I. Vardoulakis, H.J. Herrmann, D. Weatherley, P. Mora, Effect of rolling on dissipation in fault gouges, *Phys. Rev. E* 74 (3) (2006) 031306, doi:10.1103/PhysRevE.74.031306.
- [54] E. Azéma, F. Radjaï, R. Peyroux, G. Saussine, Force transmission in a packing of pentagonal particles, *Phys. Rev. E* 76 (1) (2007) 011301, doi:10.1103/PhysRevE.76.011301.
- [55] F. Alonso-Marroquín, H.B. Muhlhaüs, H.J. Herrmann, Micromechanical investigation of granular ratcheting using a discrete model of polygonal particles, in: *Simulation and Modeling of Particulate Systems, Particology* 6 (6) (2008) 390–403, doi:10.1016/j.partic.2008.07.015.
- [56] F. Alonso-Marroquín, Y. Wang, An efficient algorithm for granular dynamics simulations with complex-shaped objects, *Granular Matter* 11 (2009) 317–329, doi:10.1007/s10035-009-0139-1.
- [57] A.A. Pena, A. Lizcano, F. Alonso-Marroquín, H.J. Herrmann, Biaxial test simulations using a packing of polygonal particles, *Internat. J. Numer. Anal. Meth. Geomech.* 32 (2) (2008) 143–160, doi:10.1002/nag.618.
- [58] E. Azéma, F. Radjaï, Stress-strain behavior and geometrical properties of packings of elongated particles, *Phys. Rev. E* 81 (5) (2010) 051304, doi:10.1103/PhysRevE.81.051304.
- [59] T. Kanzaki, R.C. Hidalgo, D. Maza, I. Pagonabarraga, Cooling dynamics of a granular gas of elongated particles, *J. Stat. Mech. Theory Exp.* 2010 (06) (2010) P06020, doi:10.1088/1742-5468/2010/06/P06020.
- [60] S.A. Galindo-Torres, J.D. Muñoz, F. Alonso-Marroquín, Minkowski-Voronoi diagrams as a method to generate random packings of spheropolygons for the simulation of soils, *Phys. Rev. E* 82 (5) (2010) 056713, doi:10.1103/PhysRevE.82.056713.
- [61] J.-P. Latham, Y. Lu, A. Munjiza, A random method for simulating loose packs of angular particles using tetrahedra, *Geotechnique* 51 (10) (2001) 871–879.
- [62] A. Delaplace, R. Desmorat, Discrete 3d model as complementary numerical testing for anisotropic damage, *Internat. J. Fract.* 148 (2007) 115–128, doi:10.1007/s10704-008-9183-9.
- [63] J.-P. Latham, A. Munjiza, X. Garcia, J. Xiang, R. Guises, Three-dimensional particle shape acquisition and use of shape library for DEM and FEM/DEM simulation, *Min. Engrg.* 21 (11) (2008) 797–805, doi:10.1016/j.mineng.2008.05.015.
- [64] E. Azéma, F. Radjaï, G. Saussine, Quasistatic rheology, force transmission and fabric properties of a packing of irregular polyhedral particles, in: *Advances in the Dynamics of Granular Materials*, *Mech. Mater.* 41 (6) (2009) 729–741, doi:10.1016/j.mechmat.2009.01.021.
- [65] J.F. Peters, M.A. Hopkins, R. Kala, R.E. Wahl, A poly-ellipsoid particle for non-spherical discrete element method, *Engrg. Comput.* 26 (6) (2009) 645–657.
- [66] S.A. Galindo-Torres, F. Marroquín, Y. Wang, D.M. Pedroso, J. Castaño, Molecular dynamics simulation of complex particles in three dimensions and the study of friction due to nonconvexity, *Phys. Rev. E* 79 (6) (2009) 060301.
- [67] J. Wang, H. Yu, P. Langston, F. Fraige, Particle shape effects in discrete element modelling of cohesive angular particles, *Granular Matter* 13 (2010) 1–12, doi:10.1007/s10035-010-0217-4.
- [68] S.A. Galindo-Torres, D.M. Pedroso, Molecular dynamics simulations of complex-shaped particles using Voronoi-based spheropolyhedra, *Phys. Rev. E* 81 (6) (2010) 061303, doi:10.1103/PhysRevE.81.061303.
- [69] D. Markauskas, R. Kacianauskas, Investigation of rice grain flow by multi-sphere particle model, *Granular Matter* 13 (2010) 1–6, doi:10.1007/s10035-010-0196-5.
- [70] J. Gere, S. Timoshenko, *Mechanics of Materials*, PWS Pub. Co., Boston, 1997.
- [71] A. Taboada, N. Estrada, F. Radjaï, Additive decomposition of shear strength in cohesive granular media from grain-scale interactions, *Phys. Rev. Lett.* 97 (9) (2006) 098302, doi:10.1103/PhysRevLett.97.098302.
- [72] E. Hoek, C. Carranza-Torres, B. Corkum, Hoek–Brown failure criterion, 2002 edition, in: *5th North American Rock Mechanics Symposium and 17th Tunneling Association of Canada Conference: NARMS-TAC, 2002*, pp. 267–271.
- [73] E. Hoek, Reliability of Hoek–Brown estimates of rock mass properties and their impact on design, *Int. J. Rock Mech. Min. Sci.* 35 (1) (1998) 63–68.
- [74] A. Petri, G. Paparo, A. Vespignani, A. Alippi, M. Costantini, Experimental evidence for critical dynamics in microfracturing processes, *Phys. Rev. Lett.* 73 (25) (1994) 3423–3426, doi:10.1103/PhysRevLett.73.3423.
- [75] G. Villalobos, D. Linero, J. Muñoz, A statistical model of fracture for a 2D hexagonal mesh: The Cell Network Model of Fracture for the bamboo *Guadua angustifolia*, *Comput. Phys. Comm.* 182 (1) (2011) 188–191.
- [76] R.Y. Yang, R.P. Zou, A.B. Yu, Voronoi tessellation of the packing of fine uniform spheres, *Phys. Rev. E* 65 (4) (2002) 041302, doi:10.1103/PhysRevE.65.041302.